2013

Gold's Structural Versatility within Complex Intermetallics: From Hume-Rothery to Zintl and even Quasicrystals

Gordon J. Miller
Iowa State University, gmiller@iastate.edu

Srinivasa Thimmaiah
Iowa State University

Volodymyr Smetana
Ames Laboratory, smetana@ameslab.gov

Andriy Palasyuk
Iowa State University, palasyuk@iastate.edu

Qisheng Lin
Ames Laboratory, qslin@ameslab.gov

Gold's Structural Versatility within Complex Intermetallics: From Hume-Rothery to Zintl and even Quasicrystals

Abstract
Recent exploratory syntheses of polar intermetallic compounds containing gold have established gold's tremendous ability to stabilize new phases with diverse and fascinating structural motifs. In particular, Au-rich polar intermetallics contain Au atoms condensed into tetrahedra and diamond-like three-dimensional frameworks. In Au-poor intermetallics, on the other hand, Au atoms tend to segregate, which maximizes the number of Au-heteroatom contacts. Lastly, among polar intermetallics with intermediate Au content, complex networks of icosahedra have emerged, including discovery of the first sodium-containing, Bergman-type, icosahedral quasicrystal. Gold's behavior in this metal-rich chemistry arises from its various atomic properties, which influence the chemical bonding features of gold with its environment in intermetallic compounds. Thus, the structural versatility of gold and the accessibility of various Au fragments within intermetallics are opening new insights toward elucidating relationships among metal-rich clusters and bulk solids.

Keywords
Au, crystallographic structure, electronic structure

Comments
This conference proceeding is from *MRS Proceedings* 1517 (2013): doi:10.1557/opl.2013.45. Posted with permission.

Mater. Res. Soc. Symp. Proc. Vol. 1517 © 2013 Materials Research Society
DOI: 10.1557/opl.2013.45

Gold's Structural Versatility within Complex Intermetallics: From Hume-Rothery to Zintl and even Quasicrystals

Gordon J. Miller,[1,2] Srinivasa Thimmaiah,[2] Volodymyr Smetana,[2], Andriy Palasyuk,[1] and Qisheng Lin[2]

[1]Department of Chemistry, Iowa State University and [2]Ames Laboratory, US Department of Energy, Ames, IA 50011

ABSTRACT

Recent exploratory syntheses of polar intermetallic compounds containing gold have established gold's tremendous ability to stabilize new phases with diverse and fascinating structural motifs. In particular, Au-rich polar intermetallics contain Au atoms condensed into tetrahedra and diamond-like three-dimensional frameworks. In Au-poor intermetallics, on the other hand, Au atoms tend to segregate, which maximizes the number of Au-heteroatom contacts. Lastly, among polar intermetallics with intermediate Au content, complex networks of icosahedra have emerged, including discovery of the first sodium-containing, Bergman-type, icosahedral quasicrystal. Gold's behavior in this metal-rich chemistry arises from its various atomic properties, which influence the chemical bonding features of gold with its environment in intermetallic compounds. Thus, the structural versatility of gold and the accessibility of various Au fragments within intermetallics are opening new insights toward elucidating relationships among metal-rich clusters and bulk solids.

INTRODUCTION

Among all metallic elements, gold has the largest absolute electronegativity with a value (5.77 eV) that places it on par with the chalcogens, selenium (5.89 eV) and tellurium (5.49 eV), and the pnicogens, arsenic (5.30 eV) and phosphorus (5.62 eV) [1,2]. In the free atom, the ground state electronic configuration of gold is [Xe]$(4f)^{14}(5d)^{10}(6s)^{1}$. According to Dirac-Fock and Hartree-Fock calculations [3], the relativistic contraction of the 6*s* subshell, as determined by the ratio of expectation values of the 6*s* orbital radius evaluated with and without relativistic effects, i.e., $\langle r_{6s}\rangle_{\text{Rel}} / \langle r_{6s}\rangle_{\text{Non-Rel}}$, achieves the most extreme value for gold [4]. This relativistic contraction of the 6*s* orbital significantly lowers its energy because of the high effective nuclear charge, and results in an anomalously large first ionization potential and electron affinity for the gold atom. Since the average of these two gas-phase atomic characteristics equals the absolute electronegativity, gold's large electronegativity is a relativistic effect. Furthermore, this relativistic effect raises Au's 5*d* orbital energies and lowers the 5*d*-6*s* energy difference, both of which produce the "golden" color, as well as allow the filled 5*d* band to participate in significant polar-covalent interactions with other metals. As a result, when compared to its neighbors in the periodic table, i.e., Ir, Pt, and Hg, Au forms stronger and shorter covalent bonds to other Au atoms, as well as stronger and shorter polar-covalent bonds to other, more electropositive main group metal atoms, e.g., with In, Tl, or Sn.

The atomic characteristics of gold offer tremendous potential for its abilities to form a variety of intermetallic compounds. As one of the coinage metals, Au can form Hume-Rothery electron phases with selected metals from groups 11-14. In combination with the active alkali or

alkaline-earth metals, Au forms structures that belong to a growing number of new solids called polar intermetallics [5,6]. In these structures, the electronegative component adopts complex networks that typically optimize pairwise orbital interactions by filling bonding orbitals and keeping antibonding orbitals empty. Thus, polar intermetallics are nearly valence compounds, but, to date, no simple electron counting rules have emerged to generalize their existence. Such electron counting rules are often expressed as electrons-per-atom (*e*/*a*) ratios. Using this index, Hume-Rothery phases occur for *e*/*a* values ranging from 1.0 to 2.0. Valence intermetallics, also called Zintl-Klemm phases, belong to modified *e*/*a* values greater than or equal to 4.0 (the modified *e*/*a* value uses all valence electrons but just the atoms of the electronegative component). Polar intermetallics exist for modified *e*/*a* values between ~1.2 and 4.0. In this contribution, recent results of exploratory syntheses, structural characterizations, and electronic structure calculations for chemical bonding analysis among a variety of intermetallic compounds containing Au are summarized and reveal profound structural-chemical features.

γ-BRASSES in the Au-Zn SYSTEM

Perhaps the most structurally complex among all Hume-Rothery electron compounds are the γ-brasses, which form for *e*/*a* values around 1.61 [7]. Their structures, e.g., cubic Cu_5Zn_8, involves a bcc packing of 26-atom clusters formed by 4 concentric cages: (i) an inner tetrahedron (IT); (ii) an outer tetrahedron (OT) capping each face of the IT; (iii) an octahedron (OH) capping each edge of the OT and IT; and (iv) a distorted cuboctahedron (CO) bridging each edge of the OH. Recent extensive research into binary and ternary γ-brass systems has uncovered a need to analyze their electronic structures for chemical influences. Some of these discoveries include specific atomic ordering patterns in Cu-Zn phases [8], cubic 2×2×2 superstructures involving ordered vacancies [9,10], commensurately modulated, orthorhombic superstructures [11,12], and rhombohedral distortions for systems containing partially filled *d*-bands [13].

Our examination into the Zn-rich portion of the Au-Zn phase diagram has established the existence of rhombohedrally distorted γ-brasses occurring for 61.0-66.0 atomic percent Zn, or *e*/*a* ratios of 1.61-1.66 [14]. Au-Zn γ-brasses were obtained by allowing the elements to react at 680°C for 12 hr; then annealing for 5 days at 300°C before quenching to room temperature. According to powder x-ray diffraction, single phase products occurred for loadings that were 61.0-66.0 atomic percent Zn, and all patterns revealed a rhombohedral distortion from cubic symmetry. Results from single crystal diffraction essentially confirmed the phase relationships and lattice distortion, but provided additional structural and chemical information. In the 26-atom γ-brass clusters (see Figure 1), the IT and CO sites are Zn-rich, whereas the OT and OH sites are Au-rich, but also refine with vacancies. In fact, the vacancy concentration in the Au-Zn γ-brasses increases as Zn content increases so that the valence electron count of the 26-atom cluster (vacancies included) remains essentially constant at 41.6 electrons. Thus, the Au-Zn γ-brasses may be formulated as $Au_{5-x}Zn_{8+y}\square_{x-y}$.

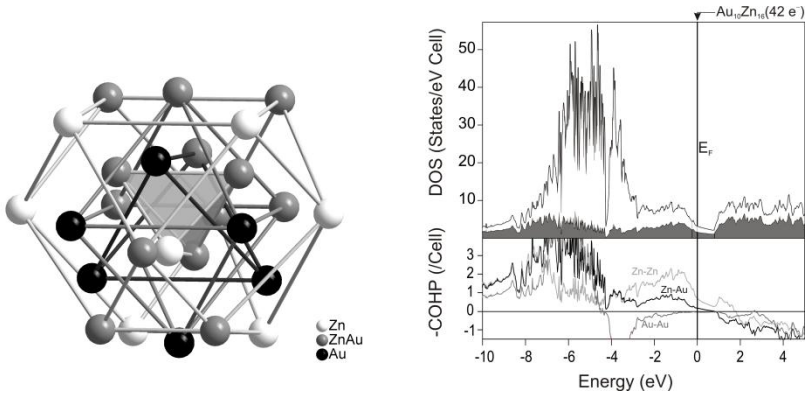

Figure 1. (Left) 26-atom cluster in Au-Zn γ-brasses. (Right) Tight-binding DOS and COHP curves evaluated for "Au_5Zn_8".

This behavior in the Au-Zn system is distinct from the Cu-Zn γ-brasses, which showed cubic phases over a wider range, i.e., 57-68 atomic percent Zn or *e*/*a* ratios of 1.58-1.72 [8]. Moreover, Cu_5Zn_8 shows complete ordering of Cu on the OT and OH sites and Zn on the IT and CO sites. Tight-binding electronic structure calculations on rhombohedral, stoichiometric "Au_5Zn_8" adopting an ordering scheme observed by experiment show a clear pseudogap in the density of states (DOS) curve at the Fermi levels (E_F) for 21-22 electrons per formula unit (42-44 electrons per 26-atom cluster) [14]. A crystal orbital Hamilton population (COHP) analysis [15] of the DOS reveals that the upper bound of this pseudogap is controlled by optimizing the Au–Zn orbital interactions. Further computational studies are needed to probe both the effects of Au/Zn atomic distributions and vacancies on the overall electronic structure and orbital interactions.

ZINTL-KLEMM INTERMETALLICS with Au

Zintl-Klemm intermetallics involve combinations of electropositive, active metals from the first two groups of the Periodic Table with electronegative (semi)metals from groups 12-15 [16]. They are also called valence compounds because the structures adopted by the electronegative components satisfy simple electron counting rules based on covalent bonding concepts, like the octet rule, once the valence electrons of the electropositive metals are formally transferred to the electronegative ones, which are called Zintl polyanions. As such, the *e*/*a* values of the electronegative components exceed 4.0. The coinage metals, Cu, Ag, and Au, alone do not form Zintl polyanions because their structures do not conform to the octet rule. Examples include the Laves-type $NaAu_2$ and KAu_2, and the hexagonal $CaCu_5$-type AAu_5 structures (A = K, Rb, Sr, Ba) [17]. Nonetheless, gold can be incorporated into Zintl-Klemm phases as a ternary component with the electron-rich group 15 semimetal Bi. In these cases, the effect of Au's filled 5*d* band becomes evident.

The recently discovered structure of Na_2AuBi, which contains planar $[AuBi]^{2-}$ ribbons [18], differs significantly from the isoelectronic compounds Li_2AuBi and NaTl (=Na_2Tl_2), which adopt the double diamond structure with 3D tetrahedral frameworks of $[AuBi]^{2-}$ and $[TlTl]^{2-}$ (see Figure 2). The $[AuBi]^{2-}$ ribbons in Na_2AuBi consist of linear Au chains with Bi atoms bridging every Au–Au contact in an alternating fashion. According to first-principles calculations, the different $[AuBi]^{2-}$ structural motifs in the Li and Na compounds are governed largely by the interplay between volume-dependent energy terms, which favor the more isotropic, 3D double

diamond structure for smaller volumes, and the covalency among the electronegative components, which favors more anisotropic, lower-dimensional motifs at larger volumes [19]. The differences between the two isoelectronic Na compounds, Na_2AuBi and Na_2Tl_2, arise from the relativistic effects and effective nuclear charges on the 5*d* states. In Na_2AuBi, Au 5*d* states significantly interact with Bi 6*p* states to promote stronger Au–Bi covalent interactions than in the diamond network. This factor does not exist for Na_2Tl_2, in which Tl 5*d* states are well localized. Thus, the relativistic effects on both the valence 6*s* and 5*d* orbitals of Au influence its behavior under reducing environments in valence compounds as well.

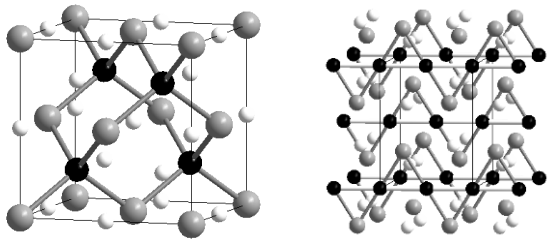

Li_2AuBi **Na_2AuBi**

Figure 2. Structures of (left) Li_2AuBi and (right) Na_2AuBi emphasizing the $[AuBi]^{2-}$ polyanions. Au: black circles; Bi: gray circles; Li or Na: white circles.

POLAR INTERMETALLICS

As mentioned above, gold and the electropositive alkali and alkaline-earth metals can form polar intermetallic compounds, which adopt structures primarily containing 3D frameworks of vertex- or face-condensed Au_4 tetrahedra. Their modified *e*/*a* ratios are 1.5 for AAu_2 (*A* = Na, K) and 1.2 for AAu_5 (*A* = K, Rb) cases [17]. Recent explorations into ternary phase spaces containing gold with an active metal and a main group *p*-metal have revealed gold's tremendous versatility to form complex structures showing numerous and distinct features of chemical bonding that range from networks to clusters and even a quasicrystal. These compounds can be semi-quantitatively indexed by a modified *e*/*a* ratio, in addition to the atomic percent Au content.

Condensed Tetrahedral Clusters

Ternary gold-rich polar intermetallics with triels (Al-Tl) or tetrels (Si-Sn) retain Au_4 tetrahedra found in binary *A*-Au phases (*A* = alkali or alkaline-earth metals). Two recently discovered alkali metal (K or Rb)-gold-trielides (In or Tl) that are especially rich in gold demonstrate typical structural features of this growing class of valence electron poor intermetallics. The structures of Rb_2Au_3Tl (modified *e*/*a* = 2.0) and K_3Au_5Tl (modified *e*/*a* = 1.83) contain, respectively, chains or sheets of Au_4 tetrahedra sharing vertices along with bridging zigzag chains of Tl to form a complex 3D network whose voids are filled by alkali metals (see Figure 3) [20]. In fact, alkali metal-gold interactions are important for the stability of these structures as seen by the arrangement of 10 alkali metals surrounding each Au_4 tetrahedron: 4 metals cap each tetrahedron face, and 6 cap each edge to give a configuration resembling the first three shells of the 26-atom γ-brass structure. Calculated electronic structures indicate pseudogaps at the corresponding Fermi levels [20], which is a feature of electronic stability among polar intermetallic compounds [21]. In these DOS curves, the Au 5*d* band falls ~4 eV

below the Fermi levels and is also ~4 eV wide to imply strongly interacting Au atoms. The position of the Au 5*d* band in the DOS curves is largely the result of each Au_4 tetrahedron being encapsulated by 10 alkali metal atoms, which engage in polar-covalent bonding with Au's filled 5*d* orbitals. COHP analyses of the DOS show that Au–In/Au–Tl and In–In/Tl–Tl orbital interactions are optimized, and account for the presence of the pseudogaps in the DOS curves. Furthermore, integrated COHP values for the different types and frequencies of interactions in these structures revealed that Au–Au and Au–In/Au–Tl interactions account for 66-75% of the total interatomic populations, while 23-24% of the total comes from K–Au/Rb–Au bonding. It is important to include the frequency of bond types in this analysis because the individual pairwise orbital interactions decrease along the sequence Au–(In,Tl), Au–Au, (In,Tl)–(In,Tl), and finally (K,Rb)–Au. Although each (K,Rb)–Au contact is the weakest pairwise interaction, the clustering of alkali metal atoms about each Au_4 group is a major factor of the overall stability of these compounds. The foregoing compounds may be usefully classified as substitutional derivatives of the cubic $MgCu_2$-type Laves phase, which occurs for $NaAu_2$.

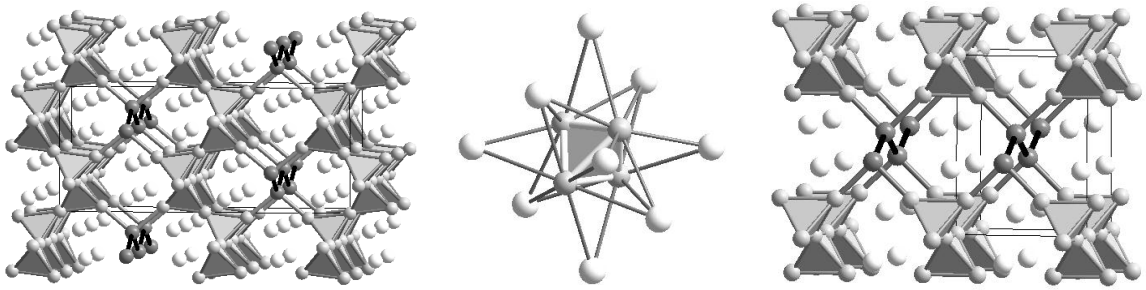

Figure 3. Two ternary Au-rich polar intermetallics, K_3Au_5Tl (left) and Rb_2Au_3Tl (right) containing condensed Au4 tetrahedra. The "Au_4A_{10}" cluster (middle) emphasizes the main Au–*A* (*A* = K, Rb) interaction.

3D Tetrahedral Networks and Networks of Icosahedra

A systematic exploration of the Sr-poor region of the Sr-Au-Al phase space has uncovered two significant structural families of polar intermetallics [22]: (i) the $Sr_x[Au_nAl_{3-n}]_yAu_{2(x+y)}$ series, which involves a 3D tetrahedral framework of Au atoms with Sr and $[Au_nAl_{3-n}]$ triangles filling the voids; and (ii) $Sr(Au_\delta Al_{1-\delta})_n[Au_{6+x}Al_{6-x}]$ phases related to the cubic $NaZn_{13}$-type, with either stuffed ($n \neq 0$) or empty ($n = 0$) icosahedra forming a simple cubic packing. All Sr-Au-Al phases were prepared by heating mixtures of the elements to 1000°C, then annealed at 750°C for 3-5 days before quenching to room temperature. Products were characterized by powder and single crystal X-ray diffraction.

In the first series, which form for 12.5-18.2 atomic percent Sr, the Au framework adopts a hexagonal diamond motif that contains an eclipsed stacking of puckered six-membered Au rings with alternating puckering modes to create short and long Au–Au distances along the stacking direction. The local environment at each Au atom in this network is a distorted tetrahedron. Moreover, the framework creates distorted hexagonal prismatic voids that are stoichiometrically half the number of Au atoms in the 3D net. Four distinct structures/phase regions have been identified that contain the 3D hexagonal net of Au atoms (see Figure 4): (i) hexagonal

$SrAu_{4+x}Al_{3-x}$ = $Sr[Au_xAl_{3-x}](Au)_4$ ($0.07 \le x \le 0.37$; modified e/a = 2.12-2.04); (ii) orthorhombic $SrAu_5Al_2$ = $Sr[AuAl_2](Au)_4$ (modified e/a = 1.86); (iii) rhombohedral $Sr_2Au_6Al_3$ = $Sr_2[Al_3](Au)_6$ (modified e/a = 2.11); and (iv) monoclinic $Sr_2Au_7Al_2$ = $Sr_2[AuAl_2](Au)_6$ (modified e/a = 1.89). The variations in lattice symmetry arise from different distribution patterns of Sr and $[Au_nAl_{3-n}]$ triangles and the compositions of these triangles, i.e., whether they are nearly $[Al_3]$ or $[AuAl_2]$. Structural refinements indicated a narrow phase width for the hexagonal $SrAu_{4+x}Al_{3-x}$ phases. In addition, detailed analyses of the orthorhombic and monoclinic structures reveal distortions of the hexagonal diamond Au network closest to those Au atoms located in $[AuAl_2]$ triangles, a result which suggests a degree of Au-Au repulsion between these sites.

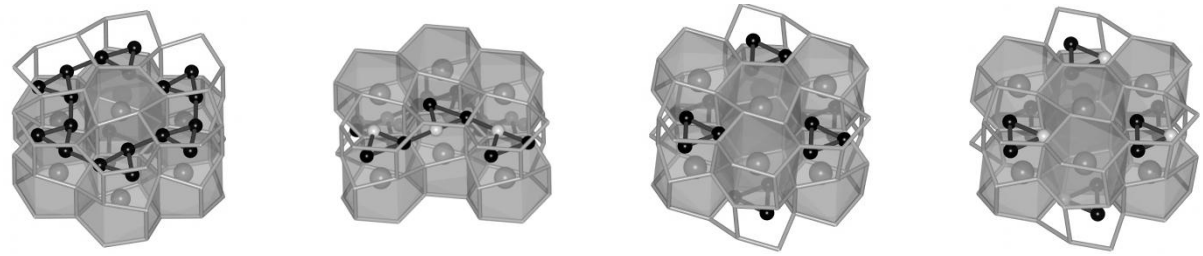

$SrAu_{4+x}Al_{3-x}$ **($P\bar{6}2m$)** | **$SrAu_5Al_2$** **(*Pnma*)** | **$Sr_2Au_6Al_3$** **($R\bar{3}c$)** | **$Sr_2Au_7Al_2$** **(*C*2/*c*)**

Figure 4. Four Sr-Au-Al structures with hexagonal 3D nets of Au atoms. Voids contain either Sr atoms (shaded) or $[Al_3]$/$[AuAl_2]$ triangles.

The valence electron concentrations for these four phase regions bifurcate into two distinct values: (1) 2.04-2.12 for the hexagonal and rhombohedral structures (i.e., those containing essentially $[Al_3]$ triangles); and (2) 1.86-1.89 for the lower symmetry cases (i.e., those containing $[AuAl_2]$ triangles). According to COHP analyses of the electronic DOS curves, the versatility of the 3D hexagonal diamond Au network arises, presumably, from the ~5 eV region of Au−Au nonbonding states near the corresponding Fermi levels for these compounds. Moreover, the hexagonal $SrAu_{4+x}Al_{3-x}$ and rhombohedral $Sr_2Au_6Al_3$ phases have most nearly optimized nearest-neighbor Au−Al and Al−Al orbital interactions with their Fermi levels falling close to pseudogaps, unlike the two lower symmetry structures. Thus, further study of their electronic structures and factors influencing their stability is warranted.

In the second series, which occurs for 7.1-7.7 atomic percent Sr and Au:Al ratios varying from 0.9 to 1.3, networks of stuffed and empty icosahedra with complex decoration patterns as well as structural transformations have been observed (see Figure 5). Cubic $NaZn_{13}$-type $SrAu_{6+x}Al_{7-x}$ phases crystallize in the range $0.60 < x < 1.25$. In these structures, Al atoms center each icosahedron, which refines as a statistical distribution of the remaining Au and Al atoms, $[Au_{6+x}Al_{6-x}]$. At lower Au content, ordered derivatives of the $NaZn_{13}$-type occur. These are either tetragonal structures with fully occupied or empty icosahedral voids, found for $SrAu_{6+x}Al_{7-x}$ ($0.30 < x < 0.60$) and $SrAu_{6-x}Al_{6+x}$ (x = ~0.25), respectively, or a completely ordered monoclinic phase $SrAu_{6.1}Al_{6.4}$. Among the Au-poor, tetragonal phases, the Au atoms are distributed on the icosahedra to maximize the number of Au−Al contacts and to minimize the number of Au−Au contacts. Monoclinic $SrAu_{6.1}Al_{6.4}$, which contains a 1:1 ordering of empty and Al-filled Au/Al icosahedra, is better reformulated as $Sr_2\{(Al)[Au_{6+x}Al_{6-x}]\}\{Au_{6-y}Al_{6+y}\}$. Trends in these structural-chemical behaviors tend to follow the Au content: the cubic phases with Al-centered icosahedra exist for 47-52 atomic percent Au; the tetragonal phases with Al-centered icosahedra occur for 45.2-47 atomic percent Au; the monoclinic phase is found for

45.0-45.1 atomic percent Au; and the tetragonal phase with empty icosahedra occurs for 44 atomic percent Au. According to preliminary electronic structure calculations, this structure-composition relationship is governed by a pseudogap in the electronic DOS curve.

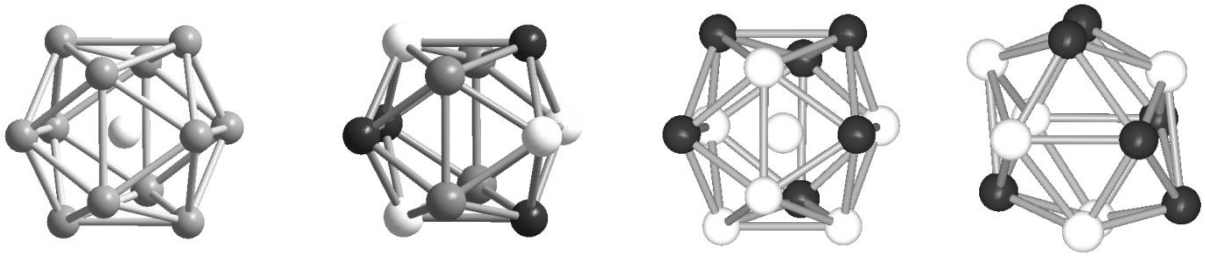

$SrAl[Au_{6+x}Al_{6-x}]$ Cubic | **$Sr[Au_{6-x}Al_{6+x}]$ Tetragonal** | **$Sr_2\{(Al)[Au_{6+x}Al_{6-x}]\}\{Au_{6-y}Al_{6+y}\}$ Monoclinic**

Figure 5. Icosahedral clusters in $NaZn_{13}$-derived Sr-Au-Al phases. Au-rich sites: black circles; Al-rich sites: white circles; Au/Al mixed sites: dark gray circles.

Weak Alkali Metal-Gold Bonding

In the previous two subsections, Au−Au and Au−*Tr* (*Tr* = Al, In, Tl) interactions as parts of clusters or networks were emphasized. But, the relativistic effects on Au's valence 5*d* and 6*s* orbitals also allow, in principle, polar-covalent interactions with alkali metals. A thorough systematic exploration of alkali metal-gold-gallium phases has identified many new compounds with diverse structural properties [23,24]. As seen for (K,Rb)-Au-(In,Tl) and Sr-Au-Al phases described above, Au atoms become incorporated into the electronegative metal framework and form numerous Au−*Tr* bonds at the expense of Au−Au bonds as the trielide (*Tr* = Al, Ga, In, Tl) content increases. One isostructural series, the tetragonal $A_{\sim 0.55}Au_2Ga_2$ (*A* = Na, K, Rb, Cs) phases [23,24], contain comparable, well-defined chains of Ga_4/Au_4 tetrahedral stars connected along the *c*-axis via direct Au–Ga and Au–Au bonds to define tunnels. These tunnels are occupied by the alkali metal atoms and consist of staggered stackings of alternant, 8-membered, planar Au_4Ga_4 rings (see Figure 6). Electronic structure calculations show a pseudogap around the Fermi levels with optimized Au−Au, Au−Ga, and Ga−Ga orbital interactions.

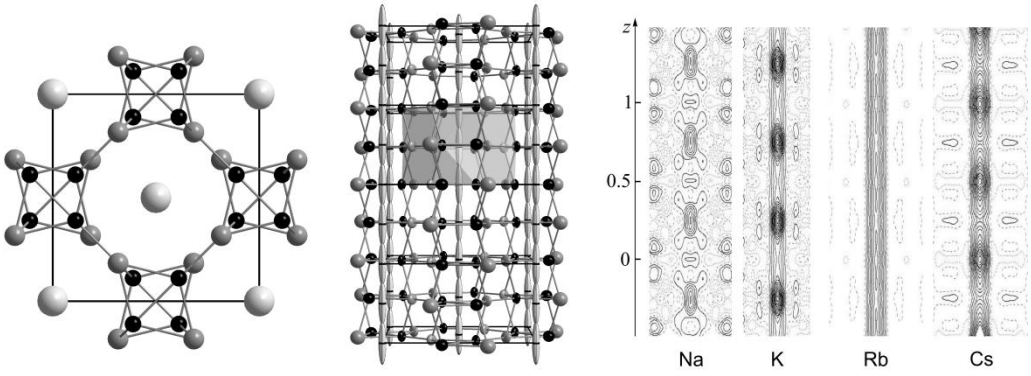

Figure 6. Crystal structure and electron densities for $A_{0.55}Au_2Ga_2$ (Au: black; Ga: dark gray; A: light gray). (Left) (001) projection; (Middle) (100) projection emphasizing elongated ellipsoids at alkali metal sites; (Right) (200) sections of electron densities along the *c*-axes.

Broad electron density peaks that are separated by diffuse electron density distributions within these tunnels result in marginal refinements of discrete alkali metal atom positions and very elongated anisotropic displacement ellipsoids (also in Figure 6). Although this outcome suggests weak alkali metal–gold bonding, the procedure fails to discriminate ranges and fluctuations of diffuse electron densities in these tunnels and, thereby, the nature of the alkali metal disorder. Electron density Fourier maps computed on the basis of observed reflection data provide more useful information about the nature of such disorder according to conventional X-ray scattering [24]. Figure 6 also shows (200) sections of electron densities along the *c* axes for $Na_{0.55}Au_2Ga_2$, $K_{0.55}Au_2Ga_2$, $Rb_{0.55}Au_2Ga_2$, and $Cs_{0.55}Au_2Ga_2$. The outlying Ga and Au atoms lie in layers at $z = 0$, ½, 1, but the atoms themselves are also alternately displaced above and below these sections, whereas the electron density maxima for Na and K clearly lie at $z \sim$ ¼, ¾ in the nominal cavities between the heavy atom layers. For Rb, the electron density appears to be nearly uniformly distributed along the cylindrical tunnel, perhaps slightly greater at $z \sim 0$, whereas Cs density is clearly greater around the planes of Au_4Ga_4 rings at $z \sim 0$, ½, 1. These characteristics suggest substantial ordering effects in which moderately rigid anionic networks define rather uniform tunnels in which the cations are somewhat loosely bound and poorly differentiated. The cations are still necessary for neutrality, and their filling of the preformed tunnel does contribute to overall stability. Changes in the lattice dimensions down the series Na-Cs are relatively small in the *c* direction (−1.0 %), but notable in *a* (+4.4 %). There is no cation location on the *c*-axis at which distances to Au or Ga atoms would be too short.

A New Quasicrystal

During further systematic explorations of the Na–Au–Ga system, the influence of significant Na–Au polar-covalent interactions became apparent along the 33 atomic percent Na line by the discovery of a new Bergman-type icosahedral quasicrystal and several crystalline approximants [25,26]. A synthetic procedure that involved initial heating to 750 °C for 3–5 hr, subsequent cooling to 350 °C for annealing over 3–5 days, and finally quenching into water yielded five new icosahedral-based structures (in order of increasing Au content): (**A**) a cubic 1/1 stuffed Bergman phase $Na_{13}Au_{18}Ga_9$; (**B**) an orthorhombic (decagonal-like) phase $Na_8Au_{10}Ga_7$; (**C**) a 2/1 Bergman approximant $Na_{13}Au_{12.5}Ga_{14.5}$; (**D**) a new quasicrystalline phase $Na_{13}Au_{12}Ga_{15}$; and (**E**) a cubic 1/1 Bergman approximant $Na_{13}Au_9Ga_{18}$ (see Figure 7). All crystalline phases were refined using single crystal x-ray diffraction. The new quasicrystal became apparent from its simple powder x-ray diffraction pattern, when compared to those for the 1/1 and 2/1 approximants **E** and **C**, as well as from initial images from a typical "single crystal" experiment, both of which could not be indexed using a conventional unit cell [26]. A more thorough investigation was carried out using a high-energy x-ray precession camera at the Advanced Photon Source at Argonne National Laboratory. The zero-level (Q_z integrated from -0.04 Å^{-1} to $+0.04$ Å^{-1}) precession images of the five-fold and two-fold planes from the sample for an incident x-ray wavelength of 0.125 Å (E = 100 keV; see Figure 7) yielded diffraction peaks that can be indexed to a primitive icosahedral quasilattice with a quasilattice constant, a_R = 5.264(4) Å, which is the largest reported quasilattice constant among icosahedral quasicrystals based on packings of Bergman clusters. The absence of extraneous spots or powder rings in these images further shows that the entire 50 μm sample corresponds to a single icosahedral grain. There is, however, some evidence of diffuse streaks in the two-fold plane that are oriented parallel to the three-fold axes of the sample [26]. This generally indicates the presence of some

degree of residual phason strain in the sample that originates from defects in tiling arrangements of the icosahedral structure.

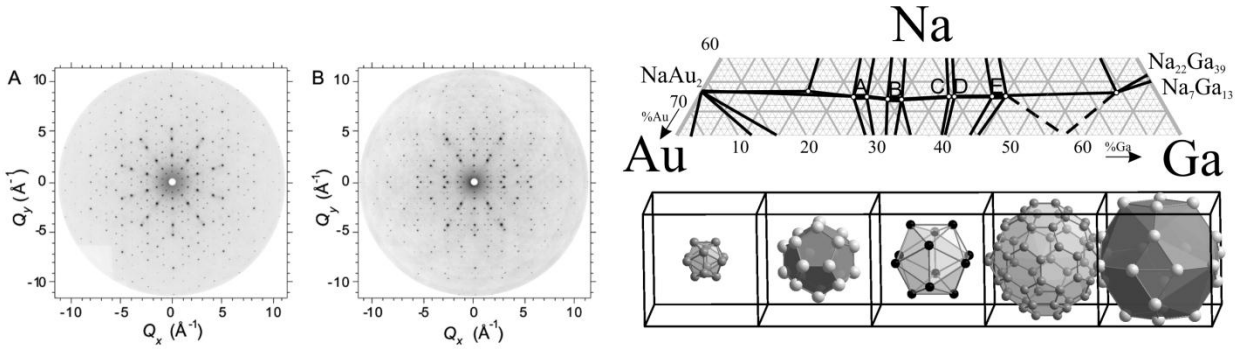

Figure 7. (Left) High-energy precession images of five-fold and two-fold planes from quasicrystal $Na_{13}Au_{12}Ga_{15}$. (Right, top) Segment of Na-Au-Ga existence diagram yielding a quasicrystal and approximants (see text for description of phases A-E). (Right, bottom) Shell structure of Bergman 1/1 approximant phase: inner Au/Ga icosahedron; dodecahedron of Na; icosahedron of Ga; truncated icosahedron of Au/Ga; polyhedral cage of Na on cubic cell boundaries.

The structure of the 1/1 Bergman approximant **E** $Na_{13}Au_9Ga_{18}$ consists of a central $(Au/Ga)_{12}$ icosahedron surrounded, in successive shells, by a dodecahedron of 20 Na atoms, a larger icosahedron of 12 Ga atoms, a buckminsterfullerene-like truncated icosahedron of a 60-atom Au/Ga mixture, and a defect triacontahedron of 24 Na atoms (see Figure 7) [25]. On the other hand, in the Au-richer 1/1 Bergman structure of $Na_{13}Au_{18}Ga_{9.5}$ **A**, certain positions that are occupied by a mixture of Au and Ga atoms in **E** become fully occupied by Au atoms and the inner icosahedron is centered by an additional Ga atom [25]. The quasicrystal **D** more closely resembles the conventional 1/1 Bergman approximant **E** with empty inner icosahedra rather than the stuffed Bergman phase **A** because (1) its composition is closer to this crystalline approximant, and (2) a comparison of the numerical relationships between the lattice parameters of these crystalline approximants and the quasilattice constant a_R confirm this assignment. According to the equation $a_{q/p} = 2a_R(p + q\tau)/(2 + \tau)^{½}$ (26), where q/p denotes the order of the approximant, τ (= $(\sqrt{5}+1)/2$) is the golden mean, and a_R = 5.264(4) Å, then $a_{1/1}$ = 14.490(11) Å and $a_{2/1}$ = 23.446(22) Å. These values fall within 3σ of the measured lattice parameters of the conventional 1/1 Bergman-type phase (i), 14.512(2) Å and the 2/1 approximant 23.460(2) Å.

The discovery of the quasicrystalline phase $Na_{13}Au_{12}Ga_{15}$ invokes questions about the special roles of Na, as well as Au, in this system. One special characteristic of $Na_{13}Au_{12}Ga_{15}$ quasicrystal is its low *e*/*a* value of 1.75, which is a value far below the favorable range for traditional Bergman-type phases (2.1–2.2) [26]. The presence of Au in the quasicrystal and approximants with Na and Ga significantly enhances aspects of metal-metal bonding and contributes to the thermodynamic stability of these phases. Accompanying theoretical studies have emphasized the relative importance of Au–*M* polar-covalent bonding, such that these interactions often comprise 65 to 90 % of the total COHP values in a specified structure. Na's participation in the delocalized metal-metal bonding, which is an important feature of any quasicrystal, remains unexpected. Clear evidence for the significant involvement of Na in bonding in the quasicrystal **D** can be extracted from the DOS and COHP curves calculated for a model 1/1 Bergman approximant "$Na_{26}Au_{24}Ga_{30}$", which use the structural parameters of **E** and the composition of the quasicrystal **D** (see Figure 8). In the DOS, Au 5*d* and 6*s* and Ga 4*s* and 4*p* orbitals make the

principal contributions to all occupied states. The Fermi level falls essentially at a sharp pseudogap, which corresponds to optimized Au–Ga and Ga–Ga orbital interactions. Of particular importance, however, is a comparison of the Na–Au and Na–Ga COHP curves, which would represent the most polar interactions in this structure. At the lowest regions of the valence band, which lies ~6.5-9.5 eV below the Fermi level, Na–Au and Na–Ga show comparable bonding interactions, with Na–Ga dominating slightly. However, the presence of the Au 5*d* band between ~6 and ~2 eV below the Fermi level greatly enhances the Na–Au orbital interactions. Analysis of all COHP curves reveals that Au–Au and Au–Ga interactions constitute, respectively, 14.7 % and 37.0 % of the total bonding population, whereas Na–Au and Na–Ga contribute, respectively, 9.3 % and 8.6 %. This contribution of the Na–Au bonding population is especially surprising and not at all in accord with classical expectations of marginal sodium covalency in such phases. Experimental, albeit more qualitative evidence for strong Na–Au bonding also arises in terms of unusually short Na–Au distances found for many of the Bergman-type crystalline phases and a few other related structures, distances which fall in the range of 3.06 to about 3.15 Å.

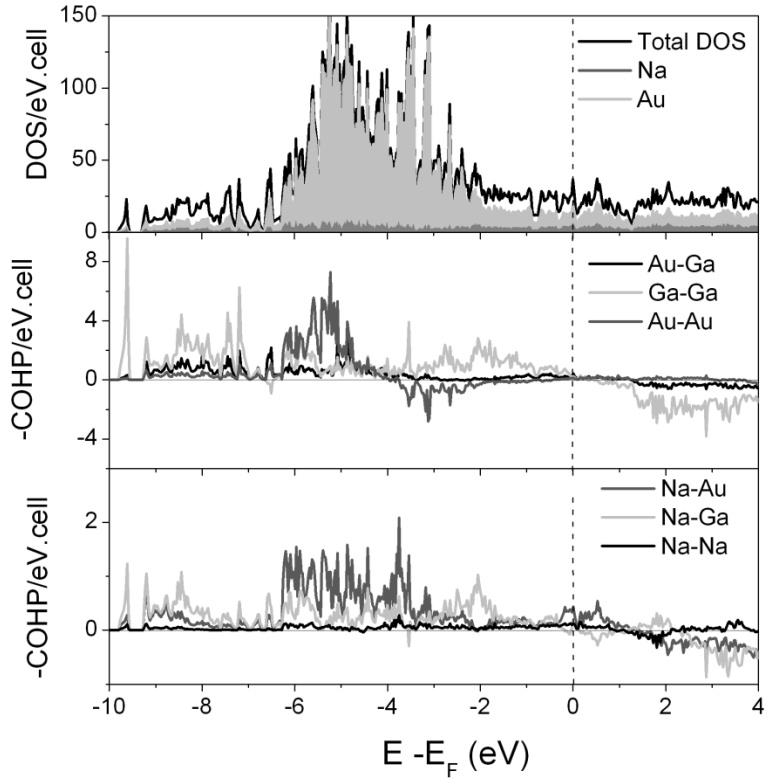

Figure 8. DOS and COHP curves evaluated for $Na_{13}Au_{12}Ga_{15}$ in the 1/1 Bergman approximant arrangement. Dotted line is the Fermi level. Shaded region in the DOS emphasizes the Au states.

Two other extraordinary examples have emerged in the Na-Au-Ga diagram [27]. Also for ~33 atomic percent Na content, the orthorhombic phase **B** $Na_8Au_{10}Ga_7$ reveals structural elements demonstrating potential local five-fold symmetry, and $Na_{17}Au_{5.9}Ga_{46.6}$ crystallizes in a rhombohedrally distorted cubic 1/1 Bergman-type approximant, differing at first in the fifth shell

of atoms. Thus, it remains whether all compounds in this Na-Au-Ga have been exposed, and these results create optimism for similar structural chemistry in many analogous systems.

SUMMARY

Gold's versatility toward adopting various structural motifs in combinations with a wide range of metallic elements is an important test of models of electronic structure and chemical bonding for intermetallic compounds. Systematic investigations of polar intermetallic systems have revealed condensed clusters, 3D networks that encapsulate small main group clusters or alkali metals, and complex frameworks leading to new quasicrystals and other complex intermetallic phases. The ability of gold to engage in homoatomic bonding as well as favorable polar-covalent bonding with various metals contributes to its versatility and provides tremendous opportunities for discovering new phases with interesting physical and possibly chemical properties.

ACKNOWLEDGEMENTS

The authors thank Profs. J. D. Corbett and A. I. Goldman for their valuable collaboration and discussions. The research in this summary was supported by the National Science Foundation, through grant DMR 10-05765, and the Office of the Basic Energy Sciences, Materials Sciences Division, U. S. Department of Energy (DOE). Ames Laboratory is operated for DOE by Iowa State University under contract No. DE-AC02-07CH11358. Use of the Advanced Photon Source was supported by the US DOE under Contract No. DE-AC02-06CH11357.

REFERENCES

1. R.G. Pearson, *Inorg. Chem.* **27**, 734 (1988).
2. L.-S. Wang, *Phys. Chem. Chem. Phys.* **12**, 8694 (2010).
3. J.P. Desclaux, *At. Data Nucl. Data Tables* **12**, 311 (1973).
4. P. Pyykkö, *Chem. Rev.* **88**, 563 (1988).
5. G.J. Miller, C.-S. Lee, W. Choe in *Highlights in Inorganic Chemistry*, Eds. G. Meyer, D. Naumann, L. Wesemann, Wiley-VCH, Weinheim, Germany (2002), pp. 21-54.
6. G.J. Miller, M.W. Schmidt, T.-S. You, F. Wang, *Struct. Bond.* **139**, 1 (2011).
7. U. Mizutani, *Hume-Rothery Rules for Structurally Complex Alloy Phases*, CRC Press, New York (2011).
8. O. Gourdon, D. Gout, D.J. Williams, T. Proffen, S. Hobbs, G.J. Miller, *Inorg. Chem.* **46**, 251 (2007).
9. S. Thimmaiah, K.W. Richter, S. Lee, B. Harbrecht, *Solid State Sci.* **5**, 1309 (2003)
10. S. Thimmaiah, G.J. Miller, *Chem. Eur. J.* **16**, 5461 (2010).
11. O. Gourdon, G.J. Miller, *Chem. Mater.* **18**, 1848 (2006).
12. J. T. Schmidt, S. Lee, D. C. Fredrickson, M. Conrad, J. Sun, B. Harbrecht, *Chem. Eur. J.* **13**, 1394 (2007)
13. O. Gourdon, S. L. Bud'ko, D. Williams, G. J. Miller *Inorg. Chem.* **43**, 3210 (2004).
14. S. Thimmaiah, G.J. Miller, *Inorg. Chem.* (2012), submitted for publication.
15. R. Dronskowski, P. Blochl, *J. Phys. Chem.* **97**, 8617 (1993).
16. G. J. Miller in *Chemistry, Structure, and Bonding of Zintl Phases and Ions*, Ed. S. M. Kauzlarich, VCH, New York (1996).

17. P. Villars, L. D. Calvert, *Pearson's Handbook of Crystallographic Data for Intermetallic Phases*, Amer. Soc. Metals: Metals Park, OH (1989).
18. S.-J. Kim, G.J. Miller, J. D. Corbett, *Z. Anorg. Allg. Chem.* **636**, 67 (2010).
19. F. Wang, G. J. Miller, *Eur. J. Inorg. Chem.* 3989 (2011).
20. B. Li, S.-J. Kim, G. J. Miller, J. D. Corbett, *Inorg. Chem.* **48**, 6573 (2009).
21. G.J. Miller, C.-S. Lee, W. Choe, in *Inorganic Chemistry Highlights*, Eds. G. Meyer, D. Naumann, L. Wesemann, Wiley-VCH: New York (2002), p. 21.
22. A. Palasyuk, G. J. Miller, to be published.
23. V. Smetana, J. D. Corbett, G. J. Miller, *Inorg. Chem.* **51**, 1695 (2012).
24. V. Smetana, G. J. Miller, J. D. Corbett, *Inorg. Chem.* **51**, 7711 (2012).
25. Q. Lin, V. Smetana, G. J. Miller, J. D. Corbett, *Inorg. Chem.* **51**, 8882 (2012).
26. V. Smetana, Q. Lin, D. K. Pratt, A. Kreyssig, M. Ramazanoglu, J. D. Corbett, A. I. Goldman, G. J. Miller, *Angew. Chem. Int. Ed. Engl.* (2012), in press.
27. V. Smetana, Q. Lin, J. D. Corbett, G. J. Miller, to be published.